AIAA Journal
Vol. 63, No. 6, June 2025

Configurational Influence on a Vortex System of a Hovering Rotor

Alexander Heintz,* Clemens Schwarz,† C. Christian Wolf,‡ and Markus Raffel§
DLR, German Aerospace Center, 37073 Göttingen, Germany

https://doi.org/10.2514/1.J064640

The blade tip vortices in the wake of a rotor are essential for the aerodynamic behavior of a helicopter. Due to the high complexity, a detailed simulation of a rotor wake is challenging and in many cases requires experimental validation. In particular, the study of secondary vortices that occur between the helically arranged blade tip vortices is part of the current research. Therefore, this paper presents an experimental study of the influence of different configurational parameters on the development of secondary vortices and their contribution to the vortex breakdown of a rotor in hover. The aim is to gain insight into which configurational parameters have an influence on the occurrence of secondary structures. An extensive database of more than 30 different configurations was created to validate the numerical simulations and methods. It was found that the blade passing frequency is the main contributor to the occurrence of secondary structures. A linear dependence between the number of secondary vortices detected and the blade passing frequency was found.

Nomenclature

BPF	=	blade passing frequency, Hz
C_T	=	thrust coefficient, $C_T = T/(\rho\pi\Omega^2 R^4)$
C_T/σ	=	blade loading
c	=	blade chord length, $c = 0.061$ m
c_{tip}	=	chord length at the blade tip, m
f	=	rotation frequency, Hz
N_b	=	number of blades
$n_{v,mean}$	=	mean secondary vortex number per 360° azimuth
Q	=	Q-criterion, s^{-2}
R	=	rotor radius, $R = 0.76$ m
r	=	radial coordinate, m
T	=	rotor thrust, N
t	=	time, s
u, v, w	=	velocity components in x, y, z directions, m s^{-1}
V_Θ	=	swirl velocity around vortex core, m s^{-1}
$V_{\Omega R}$	=	blade tip velocity, $V_{\Omega R} = \Omega R$, m s^{-1}
v_h	=	hover induced velocity, $v_h = V_{\Omega R}\sqrt{(C_T/2)}$, m s^{-1}
x, y, z	=	coordinates in the reference frame, m
Γ_v	=	vortex circulation, $m^2\,s^{-1}$
Δt	=	time delay between the particle image velocimetry double frames, s
$\Delta\theta$	=	blade-to-blade pitch angle offset, °
θ	=	blade pitch angle, °
λ_{ci}	=	swirling strength, s^{-1}
ν	=	kinematic viscosity, $m^2\,s^{-1}$
ρ	=	air density, kg m^{-3}
σ	=	rotor solidity, $\sigma = N_b c/\pi R$
$\sigma_{Gaussian}$	=	standard deviation for the Gaussian filter kernel
ψ	=	rotor azimuth position, °
ψ_v	=	vortex age, °
Ω	=	angular velocity of the rotor, s^{-1}
ω	=	vorticity, s^{-1}
ω_z	=	vorticity normal to the x, y plane, s^{-1}

Presented as Paper 2024-0896 at the AIAA SciTech 2024 Forum, January 8–12, 2024; received 16 July 2024; accepted for publication 9 December 2024; published online Open Access 24 January 2025.

*Ph.D. Student, Institute of Aerodynamics and Flow Technology, Lower Saxony; alexander.heintz@dlr.de. Member AIAA.

†Research Scientist, Institute of Aerodynamics and Flow Technology, Lower Saxony; clemens.schwarz@dlr.de.

‡Research Scientist, Institute of Aerodynamics and Flow Technology, Lower Saxony; christian.wolf@dlr.de.

§Head of Department, Institute of Aerodynamics and Flow Technology, Lower Saxony; markus.raffel@dlr.de. Associate Fellow AIAA.

I. Introduction

THE wake of a rotor is a complex three-dimensional flow, which is dominated by unsteady aerodynamic effects. In general, the wake is mainly characterized by the helix-shaped trailing blade tip vortices, the blade shear layers, the rotor-induced velocity, and the external flow conditions. The interaction of these mechanisms leads to a breakdown of the vortex system with its downward propagation. Especially, the blade tip vortices, which are initially very defined, begin to decompose with an increasing wake age. This vortex decay has been investigated for many years.

Due to its complexity, the numerical simulation of this breakdown is still challenging and therefore subject to ongoing research. The vortex decomposition is influenced by complex vortex–vortex interactions, and it is highly relevant to the efficiency and noise development of rotors, particularly in hover. Accordingly, these effects need to be investigated in detail.

In addition to the described mechanisms in the vortex system, small vortex worms, which rotate perpendicular to the primary vortex, were observed in recent high-fidelity numerical simulations. Chaderjian and Buning [1] were the first to observe the existence of these vortex worms (see Fig. 1a) and discussed whether these structures, also known as secondary vortices, trigger an earlier vortex breakdown. In later studies, the numerical observation of secondary vortices could be reproduced for many cases, e.g., by Hariharan et al. [3], Potsdam and Jayaraman [4], Öhrle et al. [5], Jain [6], and Bodling and Potsdam [7]. Despite the numerical evidence, it was debated by Egolf et al. [8], e.g., to what extent these structures are a physical or only a numerical phenomenon. Moreover, Abras et al. [9] determined a strong dependency on the numerical parameters, like time step width and grid resolution.

In 2019, Wolf et al. [2] first proved their existence in an experiment. They were able to visualize the secondary vortices with a three-dimensional Shake-the-Box Lagrangian particle tracking technique [10] (see Fig. 1b). In a subsequent experimental study, Schwarz et al. [11] quantified the appearance of the secondary vortices in a number of horizontal stereo-particle image velocimetry (stereo-PIV) planes and compared it with numerical simulations of the same test case. However, their study focused on only one specific test case. Bodling et al. [12] then used the same test case to investigate the influence of different parameters on the average amount of secondary structures. Focusing on the configurational changes, they explored the relationship between the blade tip vortex behavior and the development of secondary vortices in the numerical results. A key finding was a direct correlation between blade tip vortex breakdown and the average amount of secondary structures in the numerical simulation. Additionally, they showed that a slight offset in the pitch angle between the two blades leads to a comparable pairing behavior in the simulation and the corresponding experiment. In conclusion, the pitch offset influences both the vortex breakdown and the number

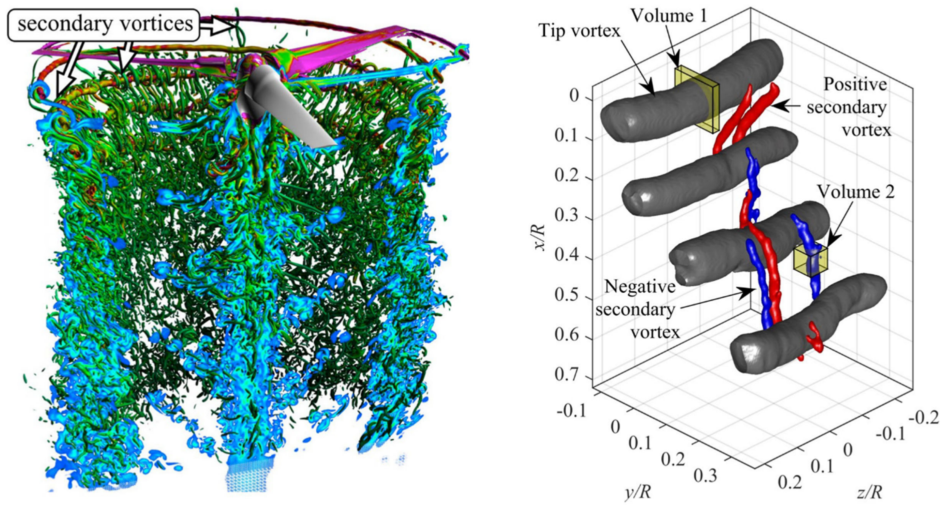

a) Adapted from Chaderjian and Buning [1]

b) Adapted from Wolf et al. [2]

Fig. 1 Previous numerical and experimental investigations of secondary structures.

of secondary structures, and it yields a better agreement between simulations and experimental results.

The recent numerical aeroacoustic study by Thurman et al. [13] indicates that initial secondary vortices also contribute to BVI noise and are therefore important for an accurate noise prediction of a helicopter.

Secondary vortices between two primary vortices are not only observed in rotor aerodynamics. In general, a distinction can be made between corotating and counter-rotating vortex pairs that lead to different shapes of secondary structures. These cases are briefly discussed below, and some interesting conclusions are explained.

Counter-rotating vortices can be observed, e.g., in the wake of a cylinder. A pair of counter-rotating primary vortices is surrounded by a secondary vortex loop, as observed by Scarano and Poelma [14], Williamson [15], and Gibeau et al. [16]. According to the work of Williamson [15], these vortices do not arise from Tollmien–Schlichting instabilities on the cylinder, but from the vortices themselves. He observed initial secondary vortices that appear to surround the cylinder. As a consequence, they cannot originate in the transition on the cylinder. The amount of the streamwise vortices along the span depends on the Reynolds number and the resulting instability mode. A detailed discussion of this phenomenon is given, e.g., by Williamson [17]. Another typical interaction case of two counter-rotating vortices is the far wake of a transport airplane in the atmosphere. Experimental and numerical investigations by Holzäpfel et al. [18], e.g., also show the appearance of secondary vortices in a similar form as described for the cylinder wake.

Corotating vortices occur in mixing layers (e.g., described by Bernal and Roshko [19]) or at crossflow instabilities during the laminar–turbulent transition (e.g., described by Wassermann and Kloker [20]). All these cases have in common that the secondary structures are S-shaped, as observed in rotor aerodynamics. For Kelvin–Helmholtz instabilities in mixing layers, Bernal and Roshko [19] suggested the origin in a three-dimensional instability of the initial shear layer. Later on, Bell and Mehta [21] could prove this suggestion. In boundary layers the origin is described as a result of a secondary instability mode of linear stability theory (LST).

Generally, corotating and counter-rotating vortices exhibit different vortex interaction mechanisms. In particular, the inner recirculation region of corotating vortices causes fluid to move around the vortices and has a strong influence on the instabilities and the flow structure in between (see Leweke et al. [22]).

The current experimental study focuses on the influence of different configurational parameters on the development of secondary vortices and their contribution to the vortex breakdown. Therefore, we used two PIV planes, one horizontal and one vertical, to detect secondary and primary vortices at the same time.

II. Experimental Setup

The experiments were conducted at the Hover Test Stand (HVG) of the German Aerospace Center in Göttingen. It is designed to investigate the aerodynamics of an isolated rotor in hover out of ground effect. This facilitates a better comparability with numerical methods, in particular for a detailed comparison of the vortex decomposition.

The rotor is mounted on a solid support structure with a built-in electric traverse system to change the height of the rotor plane. This allows for a measurement at different axial distances from the rotor without changing the PIV setups. In order to change the tip vortex spacing, the blade hub allows one to vary the blade number to one-, two-, and four-blade configurations. For the one-blade case, an approximately 12-cm-long cylindrical counterweight was mounted on the opposite side to compensate for the imbalance of the blade. To measure force and torque, a six-component piezoelectric balance is mounted directly below the propulsion system.

A. Test Rotor and Parameters

The rotor plane was between 3.1 m (4.1 R) and 3.67 m (4.8 R) above the ground, depending on the traverse height. In reference conditions, the rotor frequency was set to $f = 18.86\,\mathrm{Hz}$ or $\Omega = 118.5\,\mathrm{s}^{-1}$, respectively. The blade pitch was adjusted for a blade loading of $C_\mathrm{T}/\sigma = 0.085$, resulting in a rotor thrust of about $T = 40\,\mathrm{N}$ for the one-bladed case up to about 160 N for the four-bladed case. For the two- and four-blade cases, a variation of the blade-to-blade pitch offset was done. For the two-blade case, it is defined as the difference between the blade pitch angles:

$$\Delta\theta = \theta_{\mathrm{Blade}\,2} - \theta_{\mathrm{Blade}\,1} \tag{1}$$

The pitch offset for a four-blade case is defined as the average difference between the pitch angles of two successive blades:

$$\Delta\theta = \frac{\theta_{\mathrm{Blade}\,2} - \theta_{\mathrm{Blade}\,1} + \theta_{\mathrm{Blade}\,4} - \theta_{\mathrm{Blade}\,3}}{2}, \quad \theta_{\mathrm{Blade}\,2} \approx \theta_{\mathrm{Blade}\,4}, \quad \theta_{\mathrm{Blade}\,1} \approx \theta_{\mathrm{Blade}\,3} \tag{2}$$

An additional parameter variation covers different blade loadings C_T/σ at constant rotor frequency f, and different rotor frequencies at constant blade loading (see Table 1).

In addition to the operational parameters, the rotor blade design can have a large impact on the behavior of blade tip vortices. For this reason, we varied the blade geometry and discussed its effect on vortex decay in Sec. IV. The different geometries are presented in Table 2.

Table 1 Operating conditions

N_b	Rotation frequency, f	Blade loading, C_T/σ	Offset, $\Delta\theta$
1	$f = 18.86$ Hz, $\sqrt{2}f$, $f/\sqrt{2}$, $f/2$	f = const.: 0.059, 0.071, 0.085 $\pm$ 0.05, 0.098, 0.106	— —
2	$f = 18.86$ Hz, $\sqrt{2}f$, $f/\sqrt{2}$, $f/2$	0.085 $\pm$ 0.05	0°, 0.2°, 0.5°, 1°
4	$f = 18.86$ Hz	0.085 $\pm$ 0.05	0°, 1°

To increase the comparability with previous measurements, most test cases were performed with the SpinBlades BlackBelt 685 rotor blades, which were also used in the experimental and numerical studies of Wolf et al. [2], Schwarz et al. [11], and Bodling et al. [23]. The SpinBlades are commercially available and use a proprietary but symmetrical airfoil and a parabolic tip shape. The chord length is $c = 61$ mm, and the span is 685 mm, which, together with the rotor hub, gives a tip radius of $R = 760$ mm. The SpinBlades were used to investigate the effect of different numbers of blades ($N_b = 1, 2, 4$). To additionally analyze the effect of blade twist, the "DLR-HEL" design was introduced. The chord length and radius of the SpinBlades were kept, but the airfoil was changed to a NACA 23015 geometry, and a rectangular tip shape was used. A highly twisted blade (18° [linear], close to the optimum for hover) was compared to an untwisted blade (0°), since it was expected that the different lift distributions, and thus the different tip vortex and downwash velocities, would affect the vortex decay.

B. Particle Image Velocimetry Setup

Stereo-PIV planes provide instantaneous data of all three velocity components within a plane of the flowfield. However, only derivatives of the in-plane components can be calculated. Consequently, gradient-based vortex detection criteria are limited to vortex axes that are perpendicular to the PIV plane.

The volumetric measurements by Wolf et al. [2] (see Fig. 2a), for an instantaneous sample, indicate a spatial organization of the vortex system as sketched in Fig. 2b. To overcome the limitations of a planar, nonvolumetric measurement, the current study uses two perpendicular planes to detect the secondary and main blade tip vortices.

An alternative to stereo-PIV would be a three-dimensional particle tracking method, as in Wolf et al. [2] or Schröder et al. [24]. Unfortunately, the spatial resolution is currently not as high as for stereo-PIV. Since this research project intends to quantify secondary structures and their properties, stereo-PIV methods are preferred. As a result, the measurement setup includes two PIV planes, which were used simultaneously, as shown in Fig. 2d.

Similar setups for hover blade tip vortex investigations have been done, e.g., by Heineck et al. [25], Ramasamy et al. [26], or Mula et al. [27], and have shown the capabilities of PIV methods for blade tip vortex measurements. Schwarz et al. [11] showed the possibility to measure also the secondary structures in a horizontal stereo-PIV

Table 2 Rotor blade types

Name	Airfoil	Radius	Thickness	Chord length	Twist	Blade tip shape
SpinBlades BlackBelt	Symmetric	$R = 0.76$ m	15 %	$c = 0.061$ m	0°	Parabolic
SpinBlades BlackBelt	Symmetric	$R = 0.76$ m	15 %	$c = 0.061$ m	0°	Rectangular
DLR-HEL-0	NACA23015	$R = 0.76$ m	15 %	$c = 0.061$ m	0°	Rectangular
DLR-HEL-18	NACA23015	$R = 0.76$ m	15 %	$c = 0.061$ m	−18°	Rectangular

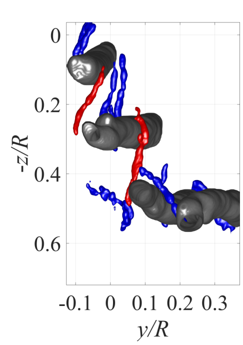

a) STB measurement adapted from Wolf et al. [2] of a vortex system with blade tip vortex pairing

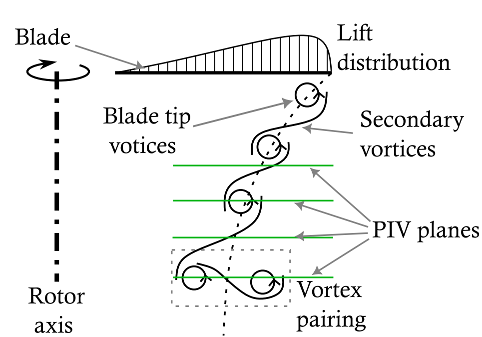

b) Scheme of the secondary structures

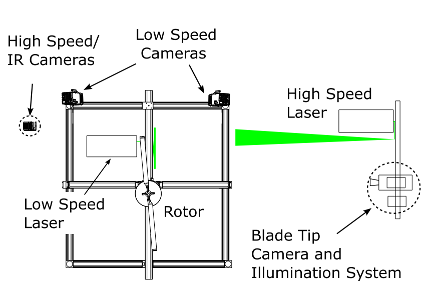

c) Top-view over the test stand and measurement devices

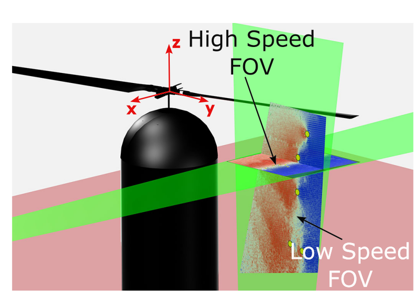

d) PIV fields of view (FOV)

Fig. 2 Sketches of the measurement systems.

plane. An overview of a wide range of important PIV measurements for rotors is, e.g., given by Raffel et al. [28].

Before describing the PIV systems in detail, the timing of each system in relation to the other is explained. For each measurement, 50 measurement cycles over one rotor revolution were performed with both systems. These are characterized by a common start at a rotor position, which is defined as $\psi = 0°$ rotor azimuth. The further recordings in each measurement cycle are then performed with the respective recording frequency. When the previous cycle has finished, the system waits until the rotor position is $\psi = 0°$ again and restarts both systems at the same rotor position.

For the horizontal plane, a high-speed PIV system was used to allow a time-resolved and statistical evaluation of the secondary vortex structures. It consists of a camera system (two Phantom VEO640L, with 130-mm-focal-length lenses and a resolution of 2080×2208 px) and a high-speed laser. The laser has an energy output of 26 mJ pulse^{-1} and a time delay between the PIV double frames between $\Delta t = 30\,\mu$s and $\Delta t = 50\,\mu$s, depending on the expected hover-induced velocity. The resulting field of view (FOV) has a size of about $0.4\ R \times 0.4\ R$ and a pixel size of 0.14 mm or equivalently, 6.93 px mm^{-1}. An acquisition frequency of 950 Hz was used to acquire 50 images per measurement cycle. This corresponds to a measurement cycle duration of $1/19$ s or the time of one full rotor revolution at the reference rotation frequency. The acquisition frequency results in a rotation of the rotor of $7.2°$ in time between the images, while the FOV covers an azimuthal range of $22.5°$ in space. In other words, each cycle covers one rotation in time to ensure an equivalent distribution in rotor phase, but at the same time, due to the overlap of the FOVs, it corresponds to approximately $22.5° \cdot 50\,\text{images} = 1125°$ azimuth of the total recorded image data. For cases with reduced rotation frequency, the number of images was increased to ensure coverage of the full azimuth range. To allow the study of different vortex ages with fixed PIV planes, the rotor was traversed vertically, resulting in FOV positions between $z/R = -0.05$ and $z/R = -0.8$ below the rotor plane.

In addition, a low-speed PIV system was used to measure the primary blade tip vortices and the overall wake structure. The location of the low-speed FOV and the camera positions are sketched in Figs. 2c and 2d. For imaging we used two pco DIMAX S4 cameras with a resolution of 2024×2024 px, equipped with 85-mm-focal-length lenses. This results an FOV with a height of about 0.9 R and a width of between 0.46 R at the top and 0.72 R at the bottom. Accordingly, an average spatial resolution of 4.85 px mm^{-1} was achieved. For illumination, we used a low-speed laser with a pulse energy of about 200 mJ pulse^{-1}. The time delay Δt was set to between $\Delta t = 50\,\mu$s and $\Delta t = 70\,\mu$s, depending on the expected hover-induced velocity for each case. The low-speed system acquired 10 images per measurement cycle with an acquisition frequency of 10 Hz. Combined with the rotation frequency of approximately 19 Hz, this results in 50 images at each of 10 different rotor phase positions.

For particle seeding, we used di-ethyl-hexyl-sebacate (DEHS) with a PIVcts1000 seeding device and filled the entire test laboratory with droplets in the diameter range of $1.2 - 2.3\,\mu$m. To achieve a homogeneous seeding, the rotor was used to distribute the particles after each seeding run. The particle images were processed with LaVision Davis 10.2 and its multigrid cross-correlation with a final window size of 16 px and a window overlap of 75 %. This results in a vector spacing of 0.58 mm for the horizontal and 0.82 mm for the vertical plane.

III. Data Evaluation and Validation

The processing of PIV data differs significantly from the usual CFD postprocessing procedure, e.g., due to the strong susceptibility of the velocity gradient calculation toward measurement noise. Given that the measurements were intended to yield a comprehensive dataset for comparison with numerical data, it is crucial to document the exact method of evaluation. This is because even minor differences in the procedure may result in substantially different outcomes.

A. Vertical FOV

The subsequent section describes the postprocessing of the vertical FOV. First, a median filter with a window size of 5 points, equivalent to 4.13 mm, is applied to remove outliers in the vector field. Second, the blades are masked based on two conditions: on the one hand, high uncertainties in the x, z plane based on the correlation statistics, described, e.g., by Wieneke [29], and on the other hand low correlation values. The mask is then slightly dilated to ensure that the whole blade is masked. Before calculating the vortex criteria for the vortex detection, it is necessary to calculate the velocity gradients. Since time resolution of 10^{-1} s is too low, gradients can only be constructed in space. For the first estimate of the vortex location, the swirling strength

$$\lambda_{ci} = \max\left[\mathfrak{I}\left\{\frac{1}{2}\left(\frac{\partial u}{\partial x}\frac{\partial v}{\partial y}\right) + \sqrt{Q}\right\}, \mathfrak{I}\left\{\frac{1}{2}\left(\frac{\partial u}{\partial x}\frac{\partial v}{\partial y}\right) - \sqrt{Q}\right\}\right] \quad (3)$$

was used.

Without any postprocessing, a typical middle-aged vortex is plotted in Fig. 3a. Due to resolution issues in the vortex core, the vortex criterion does not provide reliable data in this region. For instance, in Fig. 3a, this results in the appearance of multiple peaks for a single vortex. In addition, the gradient operator introduces noise into the vortex criterion data. To prevent false detections, a Gaussian kernel ($\sigma_{\text{Gaussian}} = 10$ points, respectively $\sigma_{\text{Gaussian}} = 8.2$ mm) was used to filter the raw swirling strength field via convolution, with a magnitude maintained by multiplication with σ. A similar approach was used by van der Wall and Richard [30] or Bauknecht et al. [31]. Bauknecht et al. [31] demonstrated that the detected center aligns with the center of the vortex void, as observed in the raw PIV images. The filtered result is shown in Fig. 3b.

The peak of the filtered data is not necessarily equivalent to the physical vortex center. Hence, a cutoff threshold of $\lambda_{ci} = 2800\ \text{s}^{-1}$ is applied, and subsequently, the resultant area is utilized to determine the center of gravity concerning the values of λ_{ci}. In instances where the blade loading varies, the threshold is scaled linearly. A comparison of the selected λ_{ci}-criterion with the Q-criterion and ω_z-criterion showed only minor discrepancies (see Fig. 3c for an example).

In addition to determining vortex positions, it is also necessary to extract the essential vortex properties. However, as the particle void is too large to detect the maximum swirl velocity for most of the vortices, this study will focus on examining the circulation. Due to the insufficient velocity data in the central void, the circulation is calculated via the line integral of the tangential velocity at a specific radius rather than via the surface integral of the vorticity. This accommodates the largest part of the total circulation while minimizing the influence of neighboring flow structures. As shown in Fig. 3d, this is only an approximation. However, it can be concluded that a radius of $r_v/c = 0.5$ does not lie within the vortex core where the circulation increases sharply with radius and is an acceptable compromise.

For each vortex, information on its position, the current rotor azimuth, the associated PIV image data, the vortex circulation, and the vortex velocity and circulation distributions over r is available and stored in a database. It contains information on 500 images taken at 10 different traverse heights. In the subsequent step, these data have to be connected to a single trajectory. This process is quite complex since the tip vortices are sometimes masked by the blades, and the youngest vortices close to the rotor plane are not within the PIV FOV, particularly for higher traverse positions.

Initially, the measurement point with the lowest rotor position, or the youngest tip vortices, is evaluated. Utilizing the current azimuth of the rotor, the initial vortices within the FOV were assigned to their corresponding original blade. Based on the order in which the vortices are arranged downstream, all other vortices of the respective instantaneous flowfields are also assigned to their vortex age. Since some vortices are still incorrectly assigned because they are obscured by blades, it is necessary to make a correction to the aforementioned assignment. This correction is predicated on the assumptions that younger vortices of the same blade are located at higher positions

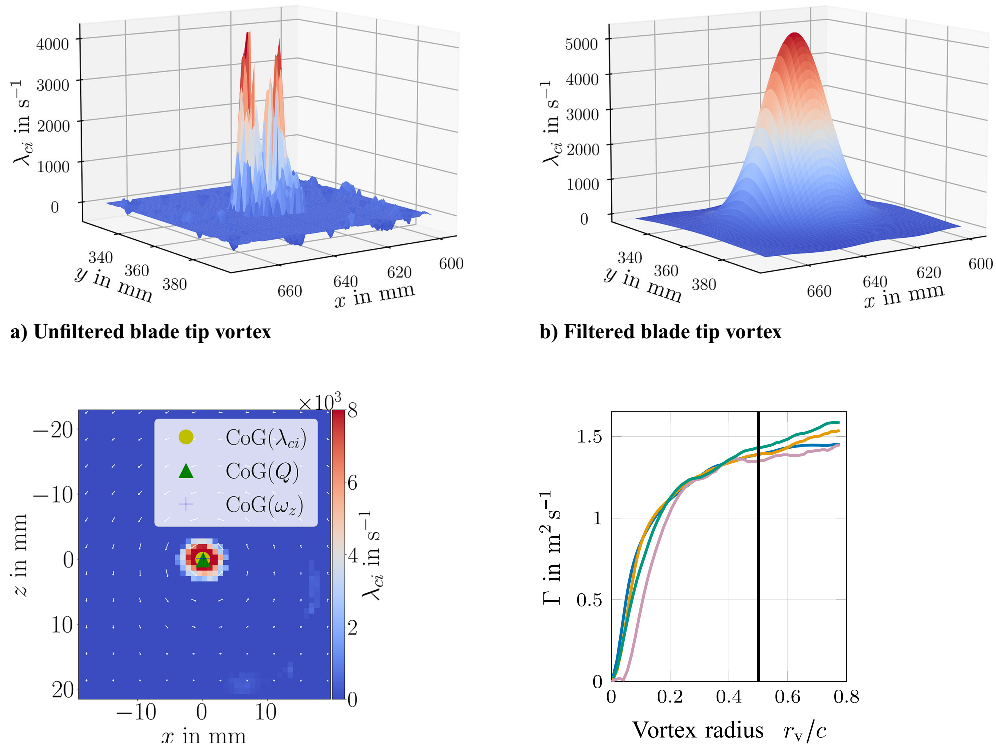

a) Unfiltered blade tip vortex

b) Filtered blade tip vortex

c) Vortex center detection based on different vortex criteria

d) Circulation Γ over the vortex radius normalized with the blade chord length *c* for several sample vortices

Fig. 3 Primary blade tip vortex detection and postprocessing.

than older ones and that vortices are only assigned to a vortex age that is too young, but not too old. To illustrate if the first vortex is obscured by a blade, it can be inferred that the second vortex has been assigned an age in the previous evaluation that is too young and does align with its height. These assumptions permit the correction of the vortex ages until a match is achieved between the age and position of the vortex. The vortex age is employed to ascertain the blades of origin. Figure 4a shows the result of this separation for a representative case involving a two-bladed rotor.

The measurement was conducted at only 10 different azimuthal rotor positions, which permitted the vortices in each instantaneous flowfield to be sorted by their current rotor azimuth angle, as shown in Fig. 4b. This illustration demonstrates that the points accumulate in point clouds in accordance with their vortex age. For each of these point clouds, the median was calculated to remove outliers, yielding a single data point for each vortex age. As a result, Figs. 4c and 4d show the median z positions of the tip vortices as a function of the vortex age and median radial positions, respectively. Due to an accumulation of mismatches in the lowest part of the FOVs, they are only evaluated to a depth of 450 mm ($-z/R = 0.59$). In the illustrations (Figs. 4c and 4d), this area is highlighted in gray.

Up to this point, only measurements taken at the lowest rotor traverse position have been evaluated. The problem with higher positions is that the youngest vortices are no longer within the FOV. In order to still be able to determine a vortex age, the high vertical overlap of the FOVs is used. The results obtained from the top FOV allow to interpolate the vortex age as a function of the height z/R. Thus, the youngest vortices of the lower FOV were assigned to a specific blade and a specific vortex age based on their height and the blade position at the time of acquisition. Finally, a fifth-order smoothing spline is applied to the calculated points to construct the vortex trajectory (see Fig. 4e).

B. Horizontal FOV

The detection of secondary vortices in the horizontal FOV is generally based on the same principles as the tip vortex detection in the vertical FOV. To remove outliers in the vector field, first a convolution median filter with a window size of nine points, respectively 5.22 mm, is applied. Due to the camera positions, the masking of the blades, which are now very present in some pictures, is crucial for the horizontal FOV. In addition to the uncertainty and correlation values, the raw images are processed to eliminate overilluminated parts of the blades that may not necessarily have a poor correlation value.

The process of detecting vortices is similar to that of the vertical FOV. The vortex detection is once again based on a vortex criterion, namely, the Q-criterion, defined as

$$Q = \frac{\partial u}{\partial x}\frac{\partial v}{\partial y} - \frac{\partial u}{\partial y}\frac{\partial v}{\partial x} - \frac{1}{2}\left(\frac{\partial u}{\partial x} + \frac{\partial v}{\partial y}\right)^2 \tag{4}$$

which was also used by Schwarz et al. [11]. It has been demonstrated to be somewhat more robust for secondary vortices. However, when similar vortex criteria are taken, e.g., swirling strength, the results did not change significantly. The flow conditions differ from those of the vertical FOV, as they involve both positive and negative vortex circulations. To differentiate between them, the Q-criterion is signed according to the sign of the vorticity and is defined as $Q_{\text{rot}} = (\omega_z/|\omega_z|)\,Q$ in the following. Even though secondary vortices exhibit a weaker particle void, Fig. 5a indicates that the Q-criterion remains quite noisy for some cases. For this reason, a Gaussian convolution filter is also used for the horizontal FOV, but with a lower standard deviation of $\sigma_{\text{Gaussian}} = 6$ pnts (or as a dimensionally affected value $\sigma_{\text{Gaussian}} = 3.42$ mm) to account for the potential spatial proximity of the structures. A representative result of this procedure is shown in Fig. 5b. For proper scaling, the filtered field is multiplied by the standard deviation. Secondary vortices are identified as coherent regions exceeding a threshold of $Q_{\text{thr}} = 48 \times 10^4\ \text{s}^{-2}$.

In Fig. 6, the influence of the Q-threshold choice on the number and circulation of the identified vortices for a two-blade sample case is observed. Figure 6a shows the significant influence on the

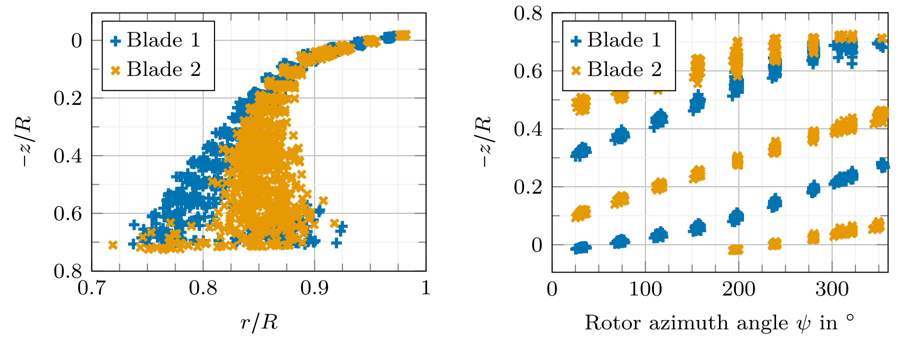

a) All detected vortices for one measurement (500 images)

b) Vortices sorted by their corresponding rotor azimuth angle

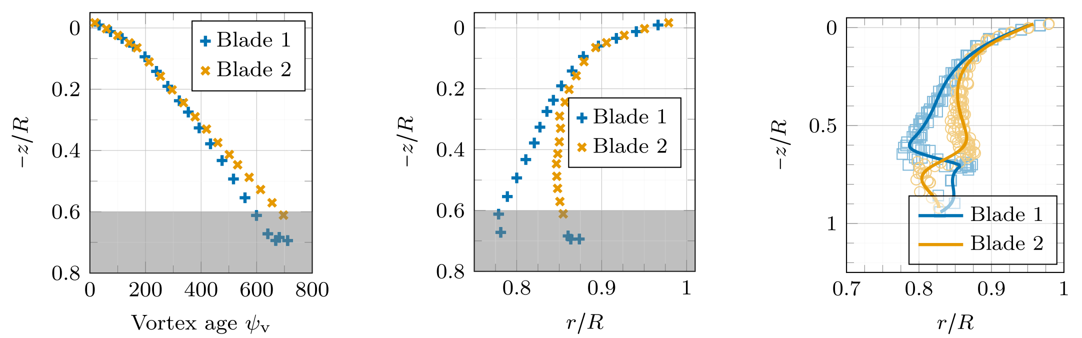

c) Averaged vortex *z*-position of the first measurement of a two-blade case plotted over the vortex age

d) Averaged vortex position of the first measurement of a two-blade case

e) Merged blade tip vortex positions

Fig. 4 Postprocessing procedure of the blade tip vortices.

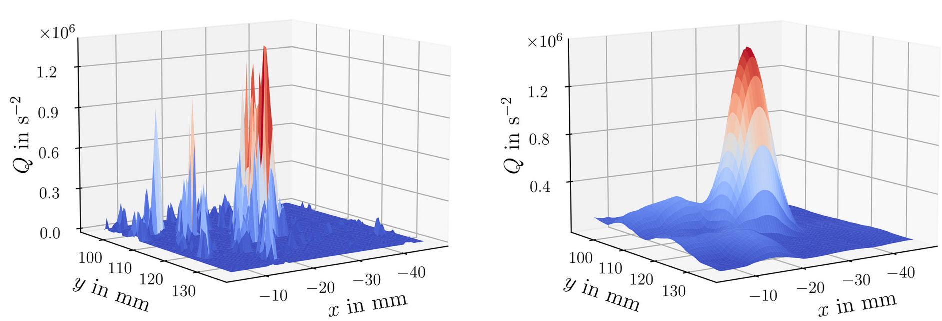

a) Unfiltered secondary vortex

b) Filtered secondary vortex

Fig. 5 Effects of filtering on the secondary vortex detection.

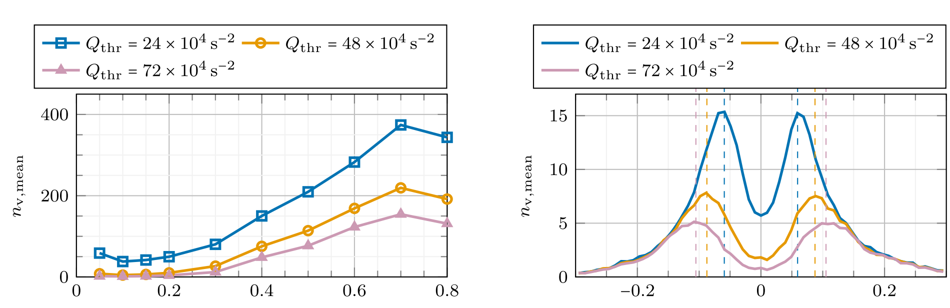

a) Sample distributions of $n_{\mathrm{v,mean}}$ over the rotor height for different thresholds

b) Histogram of the circulation distribution of the detected vortices for different thresholds

Fig. 6 Influence of the selected threshold Q_{thr}.

number of detected vortices over z/R. A lower threshold leads to more secondary structures, but there is also a risk of detecting noise or small-scale turbulence. For $Q_{\mathrm{thr}} = 24 \times 10^4\ \mathrm{s}^{-2}$, e.g., the blade shear layer is also detected at lower rotor positions. Nevertheless, different Q-thresholds at least yield qualitatively similar distributions. In order to get more insight into the vortex properties, Fig. 6b shows a histogram of the circulation of the detected vortices. For stronger vortices the circulation has no influence on the vortex number. For weaker vortices, a smaller Q-threshold results in a larger number of identified secondary vortices and a higher probability of weaker secondary vortices. A threshold of $Q_{\mathrm{thr}} = 48 \times 10^4\ \mathrm{s}^{-2}$ was found to be a good compromise between a high sensitivity but still excluding measurement noise and shear layer vortices.

To visualize the effect of filtering on secondary vortex detection, the results of a filtered and unfiltered detection are plotted over time in Fig. 7. The time axis is scaled by the blade tip vortex convection velocity to obtain a three-dimensional flowfield under the assumption of the Taylor hypothesis. There is a good agreement between the detected structures with and without the Gaussian convolution filter. However, upon comparing the green-marked secondary vortex, it appears and disappears in the unfiltered data over time. The filtering process enhances the reliability of the recognition.

For the evaluation of the secondary vortex parameters, the determination of the center of a secondary vortex is crucial. It has to be taken into account that the peak of the filtered Q_{rot} field does not necessarily coincide with the center of a vortex. Therefore, it is identified as the center of gravity of the unfiltered vorticity values in this region. Figure 8a shows in analogy to Fig. 3c that the identification of the secondary vortex centers is insensitive to the choice of the vortex criterion.

Figure 8b shows an instantaneous sample flowfield with the detected secondary structures. Since secondary vortices are part of a turbulent decay, the occurrence of them underlies a certain randomness. As a consequence, the evaluation has to be statistical with a sufficient amount of samples. For that reason, for each of the measured heights ($-z/R = 0.05$, 0.1, 0.15, 0.2, 0.3, 0.4, 0.5, 0.6, 0.7, 0.8), 2500 flowfields were measured, corresponding to more than 150 rotor revolutions in azimuth. These data are subsequently used to quantify secondary structures as a function of the wake age, respectively distance from the rotor.

Therefore, each measured field is divided into 1 deg azimuth bins to ensure an equal distribution over the measured azimuth angles. Each window must cover data up to a radius of 0.98 R for consideration. An example result is shown in Fig. 9a, wherein the gray-shaded region represents the area excluded by the first condition. In some images, the blades or reflections thereof lead to masked areas without reliable data. To address these, two rules are applied. Firstly, azimuth windows with more than 50% masking are disregarded (dark gray windows in Fig. 9b). Secondly, secondary vortices within windows with less masking are weighted using a correction factor that calculates the ratio of masked points (considered as NaN values) to the total points within this window:

$$\text{correction} = \frac{\text{number of nan values,}}{\text{number of values}}, \quad \psi_i < \psi < (\psi_i + 1) \text{ and } 0.7 < R < 0.98 \tag{5}$$

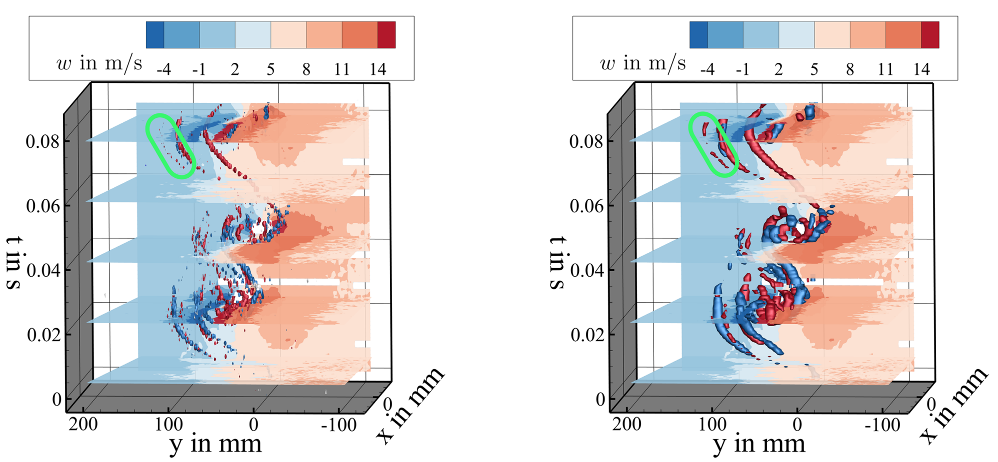

a) Raw data

b) Gaussian filtered data

Fig. 7 Secondary vortex detection sample for a one-blade test case over the time at $z/R = -0.4$ with isosurfaces of $Q_{\mathrm{thr}} = 48 \times 10^4\ \mathrm{s}^{-2}$.

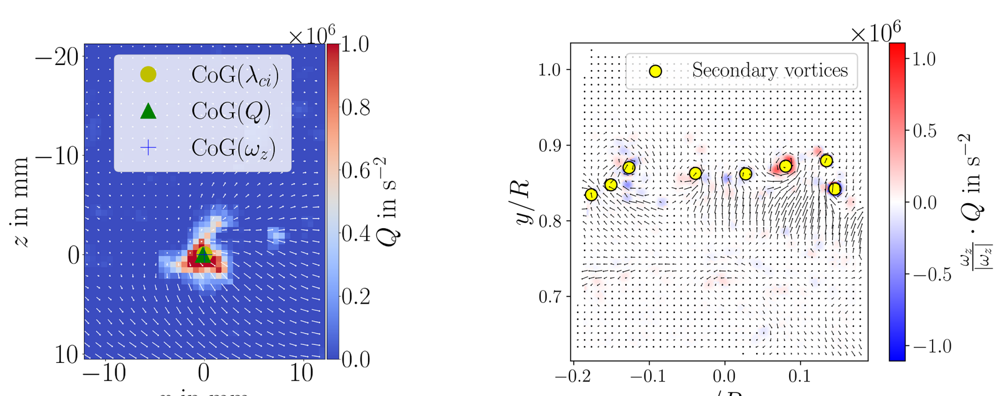

a) Vortex center detection based on different vortex criteria

b) In-plane vorticity and detected secondary structures

Fig. 8 Secondary vortex detection sample for a two-blade test case without offset, at $z/R = -0.4$.

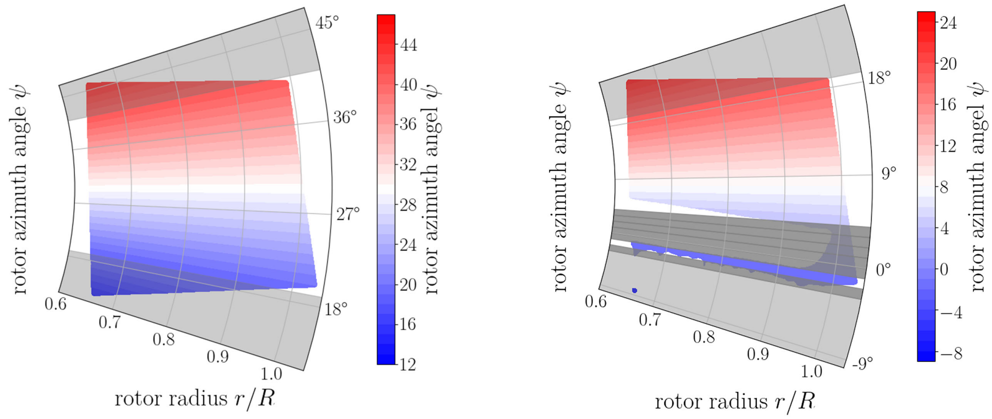

a) Azimuthal binning of the FOV. Not used areas, due to spacial limitations, are marked light gray

b) Azimuthal binning of the FOV shows light gray for unused areas due to spacial limitations and dark gray for unused bins with over 50 % mask coverage

Fig. 9 Sample FOV for statistical secondary vortex evaluation in azimuthal bins.

For each azimuthal bin with available data, the average number of secondary structures $n_{\mathrm{sec},i}$ is computed and normalized to 360° azimuth:

$$n_{\mathrm{sec},i} = \sum_{j=0}^{N_{\mathrm{windows}}} \frac{1}{N_{\mathrm{windows}}} \cdot n_{\mathrm{sec},j} \cdot (1 - \mathrm{correction}) \cdot 360° \tag{6}$$

where N_{windows} is the total number of all measured windows in the azimuthal range and $n_{\mathrm{sec},j}$ is the number of secondary structures detected in the jth window. Since the blades block always the same azimuthal region, for some azimuth angles no data exists. Under the assumption that secondary vortices appear in those regions with the same probability, the average of all azimuthal regions with data (RWD) is finally calculated as the average of all available $n_{\mathrm{sec},i}$ values:

$$n_{v,\mathrm{mean}} = \sum_{i=0}^{\mathrm{RWD}} \frac{1}{\mathrm{RWD}} n_{\mathrm{sec},\ i} \tag{7}$$

This method ensures a systematic approach to analyzing secondary flow structures while accounting for potential data limitations such as masking and blade blockage. It enables a comparison of the experimental data, which is mainly limited in the azimuthal coverage and spatially resolved numerical data. Such a comparison with a similar evaluation idea is documented by Schwarz et al. [11] or Bodling et al. [23], and its results are an elementary part of the discussion of factors influencing secondary vortices.

IV. Results

The Results section of this paper presents the analysis of configurational and operational influences on vortex decay and secondary vortex formation. It is thus organized according to configurational changes or a specific behavior of the flowfield, depending on the effect that is to be described.

A. Blade Number Influence

Airborne experiments on helicopters with different blade numbers have shown significant differences in vortex decay; see, e.g., Braukmann et al. [32]. Therefore, the first part of the discussion will concentrate on the influence of the blade number on the primary vortex breakdown. A further research question is: To what extent is the assumed early breakdown also connected to a different appearance of secondary structures?

To begin with, the focus lies on the primary blade tip vortex decay. Figure 10 shows the different behavior of the blade tip vortex trajectory. The light points in each graph represent, as shown in Fig. 4d, the average vortex position of a single measurement case and vortex age. The lines represent the regression by a fifth-order spline. A detailed documentation of the methodology of a single measurement case is in Sec. III.A. Note that the blade tip position is slightly above the hub position ($y = 0$) due to blade bending and play in the blade mounting; hence, the tip vortex trajectories may start at positive z values.

For the one-blade case (Fig. 10a) with the default blade loading of $C_{\mathrm{T}}/\sigma = 0.08$, the trajectory follows an expected trend. The initial contraction kinks due to the downward acceleration caused by the downwash of the following blade at a vortex age of about 360°. The trajectory then continues in a relatively linear path until the end of the detection. This is consistent with the observations of Quaranta et al. [33] and is explained by the extreme receptivity of helical tip vortices, where even small initial displacements are sufficient to induce long-wave vortex instabilities leading to vortex pairing. A one-bladed configuration thus minimizes the asymmetry.

The trajectory of the two-blade case (Fig. 10b), however, shows significantly more vortex interaction while maintaining a similar blade loading of $C_{\mathrm{T}}/\sigma = 0.083$. As the downwash the following blade interacts with the tip vortices, the trajectory splits into two curves. Whereas the inner vortex follows the path of the single-blade case until about $-0.5\,z/R$, the outer vortex is deflected to larger radii. This separation leads to vortex pairing at about $-0.6\,z/R$, where the two vortex paths cross. This also leads to a reduction of the distance between the paired vortices due to the downward acceleration of the outer vortex caused by the circulation of the inner one. Nevertheless, an early vortex decay in terms of no further vortex detection is not clearly seen. However, the number of older vortices decreases in comparison to the one-blade case.

For the four-blade case, shown in Fig. 10c, this interaction results in an aperiodic behavior of the vortices. Since four individual trajectories are not clearly separated due to the large spreading of each vortex path, all blade tip vortices are regressed in one curve. Additionally, the vortex decay is now earlier than for the one- or two-blade case. Nonetheless, the overall spreading of the detected vortices is less pronounced than for the two-blade case.

Comparing all regressions (see Fig. 10d), most of the vortex trajectories agree quite well. However, the pairing of the two-blade case leads particularly to a different behavior of the outer vortex part, even if this vortex interaction does not lead to an earlier vortex decay. In contradiction, the four-blade case shows an earlier vortex decay than the other two.

Focusing now on the vortex characteristics, in particular the vortex circulation, the early vortex breakdown reflects in a decrease of the circulation. Figure 11a shows for the one-blade case only a slight decrease of a nearly constant slope within the whole range of the circulation. In contrast, the four-blade case exhibits a steeper slope that further increases at around $-0.3\,z/R$. For the two-blade

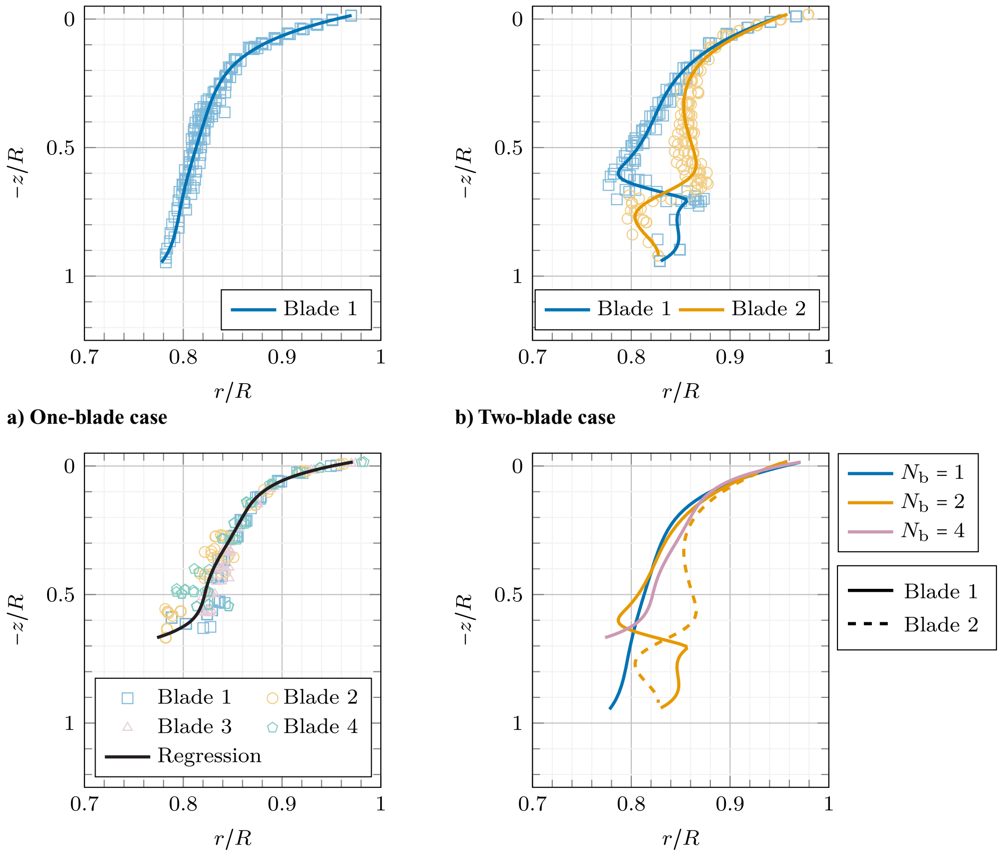

a) One-blade case

b) Two-blade case

c) Four-blade case

d) Comparison between different number of blades

Fig. 10 Example blade tip vortex trajectories for cases with different N_b.

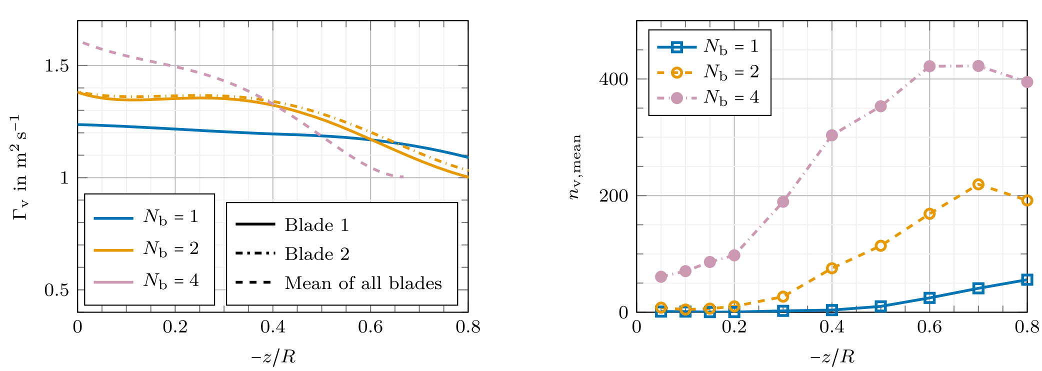

a) Primary blade tip vortex circulation Γ_v for different numbers of blades

b) Detected secondary vortices per revolution $n_{v,mean}$ for different numbers of blades

Fig. 11 Course of the primary vortex circulations for a different number of blades and detected secondary structures, with $C_T/\sigma = 0.085 \pm 0.05$.

configuration, both blades have a constant plateau up to around $-0.4\,z/R$, before the circulation starts to decrease more rapidly. The respective circulation collapse may indicate an instability process, such as vortex pairing, vortex merging, or vortex stretching; see, e.g., Leweke et al. [22]. The difference in the initial circulation is a result of the dependency of the tip loss on the number of blades, e.g., shown in the tip-loss approximation function by Betz and Prandtl [34]. A higher tip-loss factor of the circulation leads to more circulation in the trailing blade tip vortices.

Looking at the secondary structures per revolution for various numbers of blades, there is a trend of increasing detections with increasing numbers of blades. However, the collapse of the primary blade tip vortex circulation and the resulting does not correlate with an increase in detected secondary structures. Thus, newly created secondary vortices in the surrounding regions of a previous blade tip vortex are not a result of vortex fragments splitting from unstable blade tip vortices. This is evident at least in the case of a four-blade configuration. Although the number of blades has a significant influence on secondary vortices, no single parameter could be defined as the main contributor. This is because a change in the number of blades is accompanied by changes in several parameters, such as vortex distance, vortex circulation, or blade passing frequency (BPF).

B. Influence of Blade Pitch Offset

In addition to the number of blades, Schwarz et al. [11] suggested that the blade pitch offset could influence the occurrence of secondary structures. The blade pitch offset is defined as the difference between the pitch angles of the blades, whereas the mean pitch angle is kept constant. It is probable that blade-to-blade pitch differences will occur in experimental studies, e.g., as a consequence of play in the swashplate components or due to the differing elastic behavior of the blades. This is particularly relevant for handmade blades and nonisotropic blade materials, which were used in this study. Hence, a study with intentionally introduced pitch offsets is conducted, allowing to investigate their influence on the wake flow.

To demonstrate the precision and accuracy of the pitch trimming, the vortex circulation of the trailing blade tip vortices is plotted in Fig. 12a. For the trimmed case (pitch offset $\Delta\theta = 0$), the vortex circulation of blades one and two is found to be in good agreement, indicating that the pitch setting is accurate. As the pitch offset increases, the gap in between the vortex circulations of the two blades also increases.

Second, the impact on the blade tip vortex trajectories, shown in Fig. 12b, is discussed. A small offset shifts the pairing to a younger vortex age. Nevertheless, this effect is constrained to the inner vortex trajectory and quite small. Even by reversing the pitch offset, we were unable to eliminate the pairing, so the pitch offset is not the only contributing factor to vortex pairing. For example, less vortex pairing was observed for a rectangular blade shape. This is discussed in detail in Sec. IV.C.

Although a change in the pitch angle usually also leads to a change in the vortex distance, this influence cannot be observed in this experiment (see Fig. 12c). One reason for this could be that the dominance of vortex pairing forces a stable trajectory. As previously observed for the vortex trajectories, blade pitch offset does not influence the path of the trajectories significantly. Applied to the vortex spacing, the conclusion is that the vortex pairing is so dominant that it overrides other parameters such as the blade pitch. Also, an influence on the secondary vortices, shown in Fig. 12d, is not detectable. To summarize, the effect of blade pitch offset on the vortex breakdown seems not to be the driving factor.

C. Influence of Vortex Pairing

The pitch offset variation in the previous section intended to alter or suppress the tip vortex pairing and to study the resulting influence on the secondary vortices. Even though no effect was observed, we found a strong influence of the blade tip geometry on the pairing process for the two-bladed rotor, which is discussed below.

Comparing the trajectories of the rectangular blade tip shape (Fig. 13a) and the parabolic blade tip plotted in Fig. 13b, the rectangular blade tip shape leads to much less pairing up to about $-0.6\,z/R$. One possible reason for this is instabilities in the blade tip vortex generation.

In general, the wingtip vortex is the result of a merging and roll-up of multiple discrete vortices that emerge due to the infinitesimal changes in circulation (see, e.g., Luckring [35]). Following this idea, the trailing blade tip vortices of a parabolic blade tip shape should be merged over the length of the tip. Since the rectangular blade ends abruptly, this process is constrained to a limited radial range, and consequently these vortices should be more defined. Finally, it can be assumed that this leads to fewer introduced instability modes than for the parabolic blade tip. An alternative hypothesis is a change of the vortex core size due to the blade tip. From generic experiments on corotating vortices, it is known that the core size is an important factor for vortex interaction and vortex pairing mechanisms (see Meunier and Leweke [36]). However, this was not the primary objective of the investigation, and the measurement system was not designed to provide a detailed velocity field for very young blade tip vortices. This would require a higher spatial and temporal resolution of the near-field wake.

Before comparing the detected number of secondary vortices, Fig. 13c proves that there is no considerable impact on vortex circulation in the rotor wake due to the change in lift distribution over the blade due to the tip-shape change.

Although the current study lacks a comprehensive analysis of the relation between tip shape and vortex stability, this case provides a basis for comparison of the extent to which the occurrence of secondary vortices is influenced by vortex interaction. Figure 13d shows that this influence seems negligibly small. Figure 2b introduced the concept that secondary vortices are more likely to occur in the vicinity of primary vortices. Vortex pairing means that the two primary vortices, e.g., in the two-blade case, no longer lie in a plane with a 180° phase shift but move azimuthally closer to each

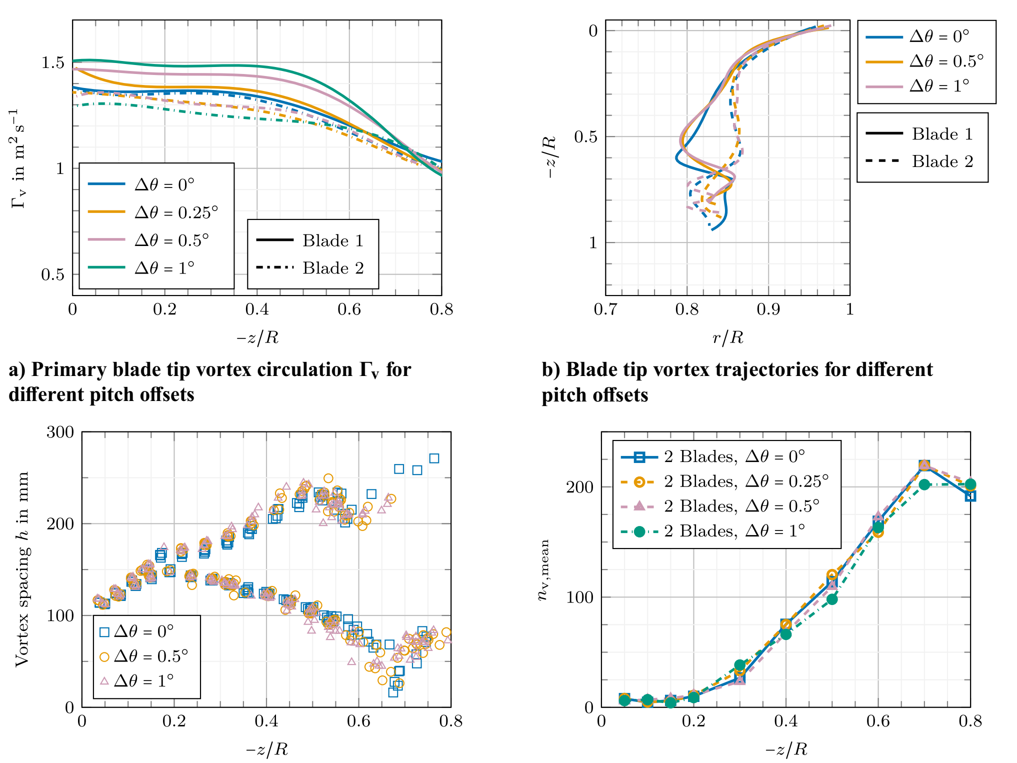

a) Primary blade tip vortex circulation Γ_v for different pitch offsets

b) Blade tip vortex trajectories for different pitch offsets

c) Average blade tip vortex distance for each illuminated azimuth in each conducted measurement over the mean z-distance

d) Detected secondary structures and course of the primary vortex circulations for different pitch offsets

Fig. 12 Influence of blade pitch offset $\Delta\theta$ on blade tip vortex characteristics and secondary vortex appearance.

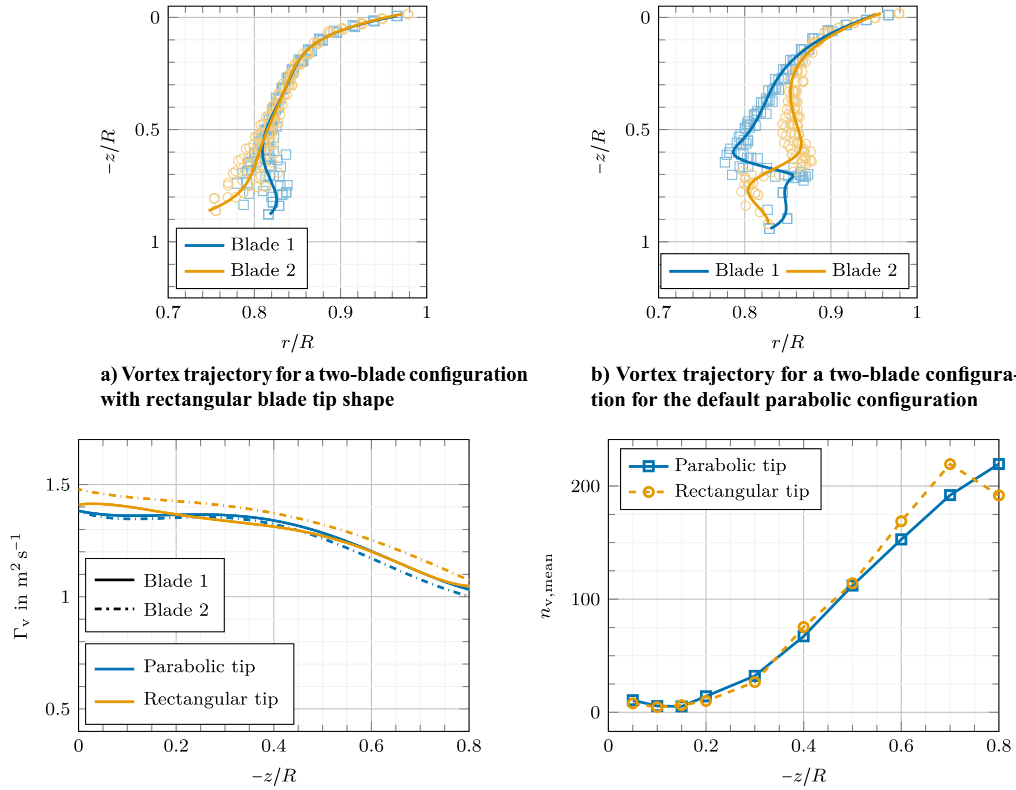

a) Vortex trajectory for a two-blade configuration with rectangular blade tip shape

b) Vortex trajectory for a two-blade configuration for the default parabolic configuration

c) Primary blade tip vortex circulation Γ_v for different blade tip shapes

d) Detected secondary structures for different blade tip shapes

Fig. 13 Comparison between a case with strong vortex pairing (parabolic blade tip shape) and with weak vortex pairing (rectangular blade tip shape).

other. Consequently, the secondary vortices should also be distributed differently in the azimuthal domain, despite a similar total number.

Figures 14 and 15 indicate that this generalization is accurate. At $-0.2\,z/R$ (Figs. 14a and 15a), for both blade tip shapes, there are two peaks of secondary vortices with about 180° phase shift, which also can be observed for the two azimuthal positions of the blade tip vortices marked in orange and blue. These are the azimuth positions at which the tip vortices cross this z/R plane, as observed by the vertical PIV planes. The parabolic blade tip, as shown in Fig. 14b, which displays the results at a height of $-0.8\,z/R$, demonstrates the influence of pairing, causing a reduced phase shift from approximately 180° to about −40°, meaning that the tip vortices switched places. Regarding the distribution of the secondary vortices, the two

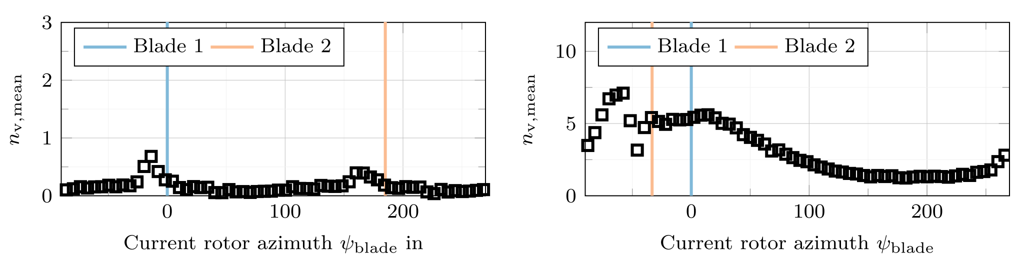

a) $z/R = -0.2$

b) $z/R = -0.8$

Fig. 14 Azimuthal distribution of secondary vortices and the corresponding positions of the blade tip vortices for a case with strong vortex pairing (parabolic blade tip shape).

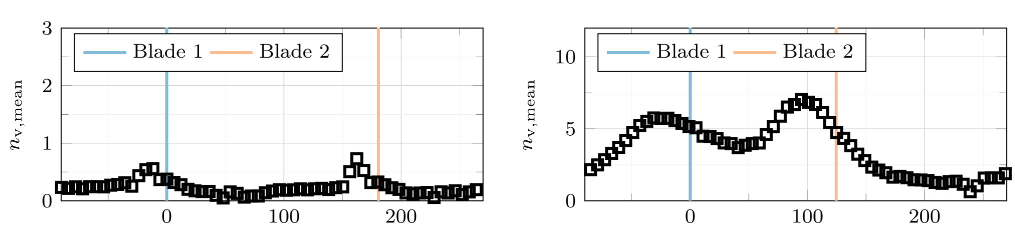

a) $z/R = -0.2$

b) $z/R = -0.8$

Fig. 15 Azimuthal distribution of secondary vortices and the corresponding positions of the blade tip vortices for a case with weak vortex pairing (rectangular blade tip shape).

peaks merge as the primary vortices are nearly in the same plane. For the blade with the rectangular tip, a much smaller phase shift from approximately 180° to about 125° can be observed in Fig. 15b. This is mainly the result of the weak vortex interaction in this case. Accordingly, the two separate peaks of detected secondary structures also remain. Finally, a clear influence of vortex interaction on secondary vortices can be seen, in terms of not their number $n_{\mathrm{v,mean}}$ but their azimuthal distribution.

D. Influence of Blade Loading

At this point, the effect of the number of blades on the secondary vortices is investigated. So far, it was found that neither a blade pitch offset nor a blade tip vortex interaction is the driving factor for the occurrence of secondary vortices. For this reason, the next investigation is done using a single-bladed rotor with varying blade loading to investigate the effect of blade tip vortex spacing. As it was unclear to what extent the influence of vortex interactions is negligible, the investigations were mainly carried out on a one-blade rotor with the object of minimizing the potential impact of vortex interactions.

Figure 16a shows the tip vortex spacing of the one-bladed rotor for various blade loadings and as a function of the z position. Although a considerable variation was achieved, the comparison with Fig. 16b shows that the variation is still smaller than for the variation of the number of blades. Nevertheless, the variation of the tip vortex spacing in Fig. 16a is sufficient to study its influence on the number of secondary vortices (see Fig. 16c). A reduction in blade loading, which is accompanied by a decrease in vortex spacing, results in a greater number of secondary vortices. Even if the effects are not as large as those of changing the number of blades, the influence on secondary structures is present. Although it does not seem to be the primary factor influencing the differences in secondary structure occurrences between the different number of blades, it is certainly a subordinate factor.

E. Influence of the Blade Geometry

Until now, this paper has only focused on a single-blade geometry in its investigations. In this section, we will discuss the impact of blade design variation on secondary vortex decay. As shown in Table 2, the blade design was modified to a generic own design with a lift-producing airfoil (NACA23015) in contrast to the symmetric airfoil (SpinBlades parabolic and rectangular). The own designs have a rectangular tip shape and have been measured with a linear twist of −18° (DLR-HEL-18) and again in an untwisted version (DLR-HEL-0). The design objective of these generic blades is to use a well-known airfoil together with an easily reproducible geometry.

Figure 17a shows the trajectories of the DLR-HEL blades in comparison with the SpinBlades parabolic blade. The DLR-HEL-0 has a slightly higher contraction. A possible explanation is the doubled airfoil moment coefficient of the NACA 23015, compared to the symmetric SpinBlades airfoil, resulting in a higher torsion toward negative twist. A negative twist leads to a reduction in thrust at higher rotor radii and, as a result, a higher contraction. This impact of twist is also seen with the prescribed wake model by Kocurek and Tangler [37]. For the DLR-HEL-18, the twist is even higher, which explains the higher contraction of the blade tip vortex trajectory that was observed.

Regarding the vortex circulation, which is plotted in Fig. 17b, it is obvious that the high twist of the DLR-HEL-18 blade leads to a weaker pressure gradient at the rotor tip, resulting in a reduced vortex

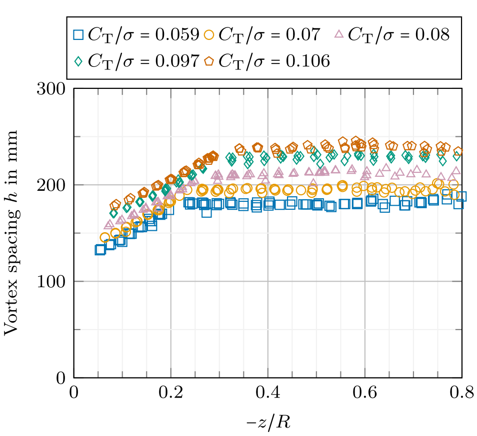

a) Average blade tip vortex distance for each illuminated azimuth in each conducted measurement over the mean z-distance for different blade loadings C_T/σ

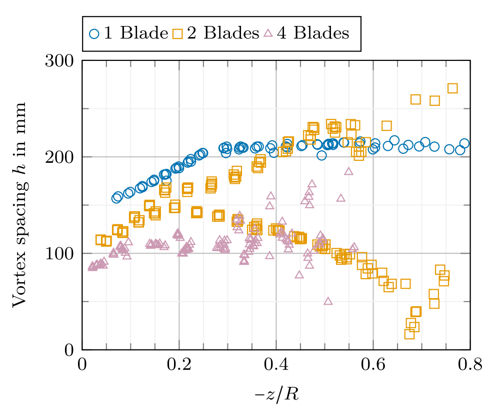

b) Average blade tip vortex distance for each illuminated azimuth in each conducted measurement over the mean z-distance for different number of blades N_b

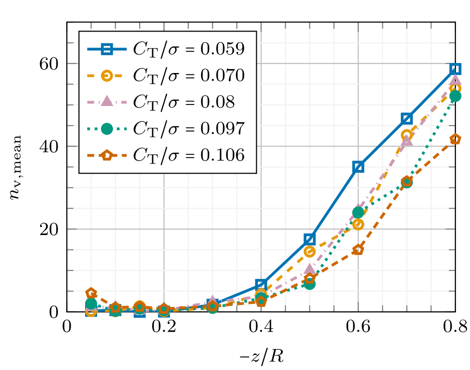

c) Detected secondary structures for different blade loadings C_T/σ

Fig. 16 Influence of blade loading C_T/σ on blade tip vortex characteristics and secondary vortex appearance.

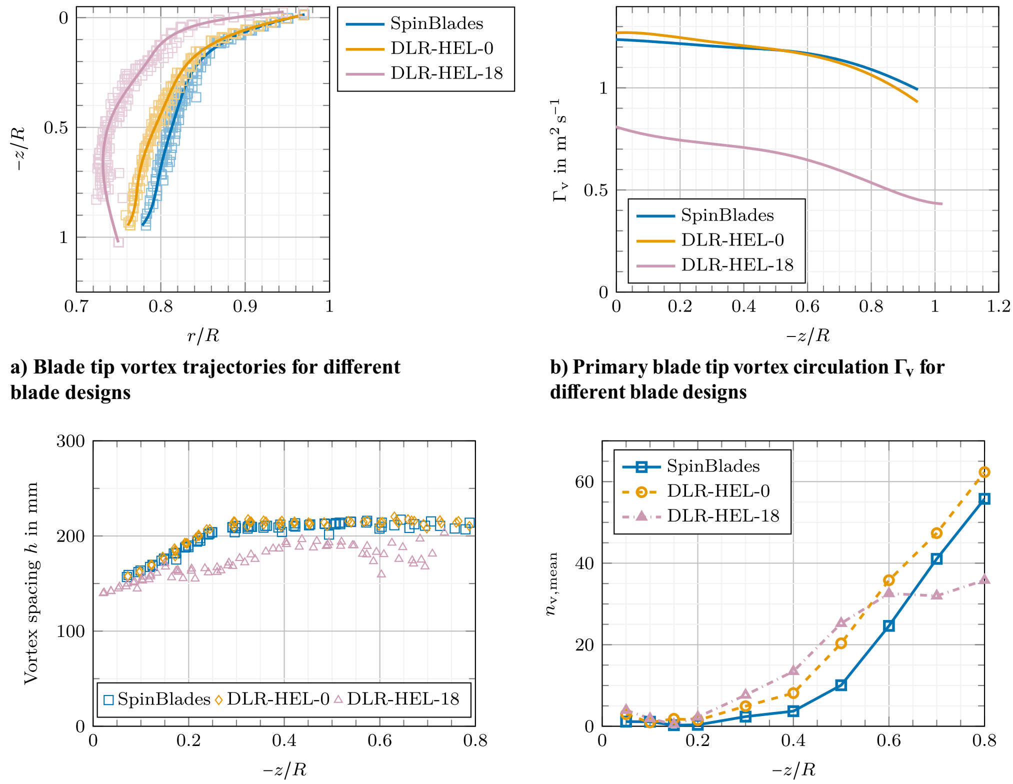

a) Blade tip vortex trajectories for different blade designs

b) Primary blade tip vortex circulation Γ_v for different blade designs

c) Average blade tip vortex distance for each illuminated azimuth in each conducted measurement over the mean z-distance for different blade designs

d) Detected secondary structures for different blade designs

Fig. 17 Influence of various blade designs on blade tip vortex characteristics and secondary vortex appearance for a one-blade case.

circulation. For the untwisted blades, DLR-HEL-0 and SpinBlades, the course of the vortex circulation is very comparable. The slight discrepancy in the initial circulation is a result of the influence of the blade geometry toward a change in the lift distribution.

The reduced circulation on the outer part of the DLR-HEL-18 rotor is also noticeable in the vortex spacing shown in Fig. 17c. In contrast to the SpinBlades and the DLR-HEL-0 rotor, which exhibit identical vortex spacing over the entire vortex age, the DLR-HEL-18 has a significantly smaller vortex spacing, particularly within the range between $-0.2\,z/R$ and $-0.4\,z/R$. Interestingly, however, this approaches the level of the other two rotor blade designs for larger vortex ages.

Figure 17d shows a clear influence of the blade design on secondary structures. Both DLR-HEL rotor designs show a higher number of secondary vortices at rotor distances up to about $0.5\,z/R$. For older vortices, however, the DLR-HEL-18 no longer shows an increase in the further course and thus even has fewer detected structures from $-0.7\,z/R$ onward. This can be attributed to the earlier onset of vortex decay for this blade. Conversely, the DLR-HEL-0 continues its course parallel to the SpinBlades configuration up to the oldest detected position. This shows the dependence of vortex decay and secondary vortex occurrence on the specific rotor design.

F. Influence of the Blade Passing Frequency

Up to this point, this paper showed various parameters with varying degrees of influence on secondary structures, but it was not possible to identify a single driving parameter, which allows us to compare cases with different numbers of blades. Subsequently, the BPF was evaluated, and additional measurements were conducted in order to allow for the same BPF for one- and two-blade cases. The blade loading remains constant with a pure variation of the rotation frequency. The one-bladed BPFs are 13.37 Hz, 18.86 Hz, and 26.68 Hz, and the two-bladed BPFs are 18.9 Hz, 27.02 Hz, and 37.7 Hz. This allows for a comparison of the one- and two-bladed configurations at two different BPF levels. The upper limit for the BPF was given by mechanical restrictions of the setup and power limitations of the propulsion system. To show a more complete picture of the influence of the BPF, we additionally present data for the one-blade case 13.37 Hz and for the two-blade case 37.7 Hz, despite the absence of corresponding comparative data.

The results of the secondary vortex detection are shown in Fig. 18a. One-bladed data are shown in blue, whereas two-bladed data are shown in orange. The number of secondary vortices increases with an increasing BPF. The one- and two-bladed cases yield very similar values at the same (or similar) BPF. By tendency, the two-bladed rotor produces slightly more secondary vortices. It is noted that the BPF does not affect the vortex spacing (see Figs. 18c and 18d). For the one-bladed case, the spacing is constant over the BPF. It is important to highlight that this includes cases with both similar and dissimilar Reynolds and Mach numbers. When varying the number of blades, these parameters remain constant while the thrust coefficient C_T changes. Conversely, when the rotation frequency f is adjusted, C_T is held constant, resulting in variations in the blade tip Reynolds and Mach numbers. For the two-bladed case, the trajectory split caused by the vortex pairing is apparent, but the BPF variation results in some scatter but no systematic trend. In summary, the time constant between two successive blade passes is an independent and decisive parameter of secondary vortex formation.

Having established that the BPF has a major influence on the occurrence of secondary vortices, Fig. 18b now shows all measured secondary vortices at a height of $-0.6\,z/R$ above the BPF. For the observed range, a nearly linear dependency from the BPF is shown. However, it is noticeable that the origin of this linear line is not at BPF $= 0$ Hz. This is due to the fact that very small-axis or weak structures are not detected by the measurements. In cases with a small BPF and low thrust, the secondary vortices are below this detection threshold.

Figure 19a shows the regression curves of the BPF of all cases for other distances to the rotor plane. For small distances,

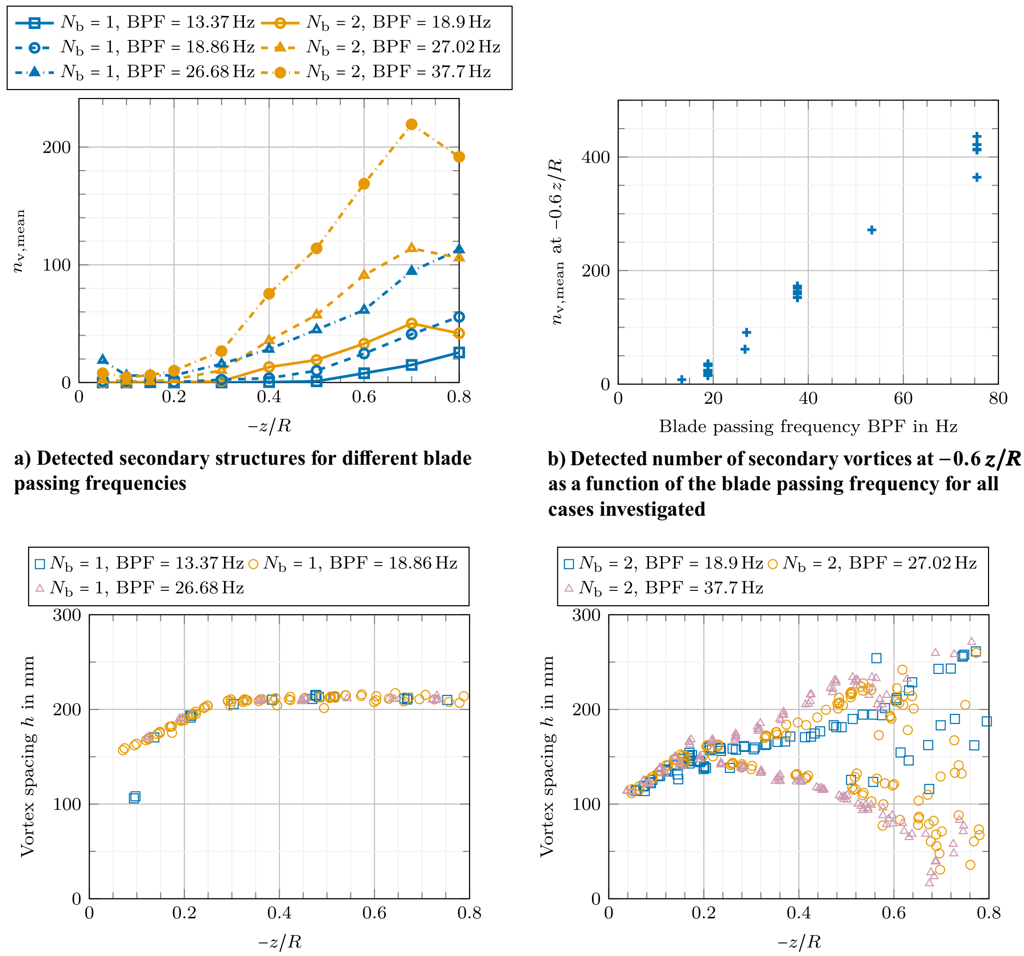

a) Detected secondary structures for different blade passing frequencies

b) Detected number of secondary vortices at $-0.6\,z/R$ as a function of the blade passing frequency for all cases investigated

c) Average blade tip vortex distance as a function of the z-coordinate for different BPFs for $N_b = 1$

d) Average blade tip vortex distance as a function of the z-coordinate for different BPFs for $N_b = 2$

Fig. 18 Influence of BPF on blade tip vortex characteristics and secondary vortex appearance.

it seems to be a more exponential curve, and for rather large distances ($0.7\,z/R$ and $0.8\,z/R$) and blade passing frequencies, the amount of secondary vortices is below the estimated curve. The reason for this is the incipient decay of primary and secondary vortices, which starts earlier for higher BPF than for lower ones. Nevertheless, the general statement of the strong dependence of secondary vortices for the BPF holds true for any measured distance under the condition that vortex decay plays a minor role.

In Sec. III.B, it was argued why a detection threshold of $Q_{\mathrm{thr}} = 48 \times 10^4\ \mathrm{s}^{-2}$ seems to be a reasonable compromise for evaluation purposes. To further evaluate its influence on the key results, a parameter variation was done for each case, and the resulting secondary vortices at $0.6\,z/R$ over the BPF are plotted in Fig. 19b. As expected, a lower threshold leads to a higher number of secondary vortices detected in each case. However, the factor in between $Q_{\mathrm{thr}} = 72 \times 10^4\ \mathrm{s}^{-2}$ and the other evaluations varies with the BPF (see Fig. 19c). Cases with smaller BPF values are more sensitive to threshold variation, which means that these cases contain smaller structures than those with higher blade passing frequencies. There seem to be two main explanations for this trend. First, the initial number of secondary vortices for small blade passing frequencies is quite small. As a consequence, almost all secondary vortices lie below the detection threshold. Second, with a limited resolution of an FOV, there are also a limited number of separate secondary vortices that can be detected. A result of the threshold decrease is that several vortices may be detected as they are on a plateau with no decrease in Q in between. A physical vortex merging and an apparent merging due to the limited resolution cannot be separated.

V. Conclusions

Overall, this paper presents the measurements on the HVG, which allows for measurements on vortex decay of rotors in hover without tail rotor or fuselage interaction. This enables the isolated observation of vortex decay processes with as few interactions as possible in order to facilitate numerical comparison. Two PIV planes were evaluated to capture both the main blade tip and secondary vortices. To create a comprehensive database for the validation of numerical simulations, over 30 different configurations were investigated and showed the configurational influence on vortex decay, vortex properties, and the occurrence of secondary structures. This also makes it possible to compare the extent to which primary and secondary vortices influence each other.

Most notable is the influence of the BPF on vortex decay and, in particular, on secondary structures. The results show that this influencing factor significantly determines the occurrence of secondary vortices. An almost linear relationship was found for the number of secondary vortices as a function of the BPF for all the variants presented. This shows why the number of rotor blades has a significant influence on secondary vortices. However, also other variations, such as the used airfoil, blade twist, and blade loading, also have an effect on secondary vortices and blade tip vortex decay.

In addition to the parameters that have an effect on secondary vortices, it is also important to mention the investigated parameters that have no effect. Neither blade-to-blade pitch offset nor vortex pairing has any effect on the amount of secondary structures. This is all the more noticeable in the case of vortex pairing, as the azimuthal distribution of the secondary vortices changes as expected.

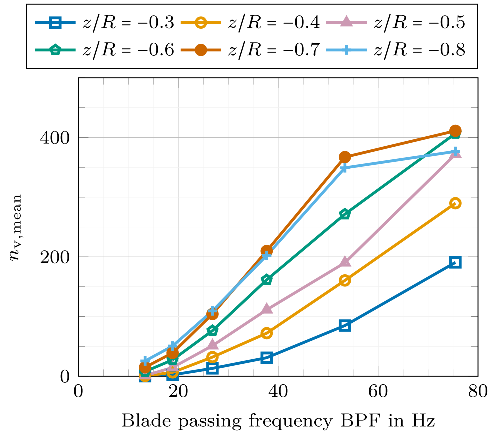

a) Regressions of the detected number of secondary vortices for several distances to the rotor plane as a function of the blade passing frequency

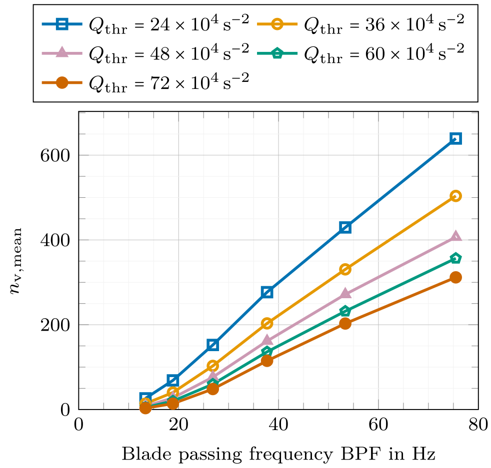

b) Regressions of the detected number of secondary vortices at $-0.6\,z/R$ for different detection thresholds as a function of the blade passing frequency

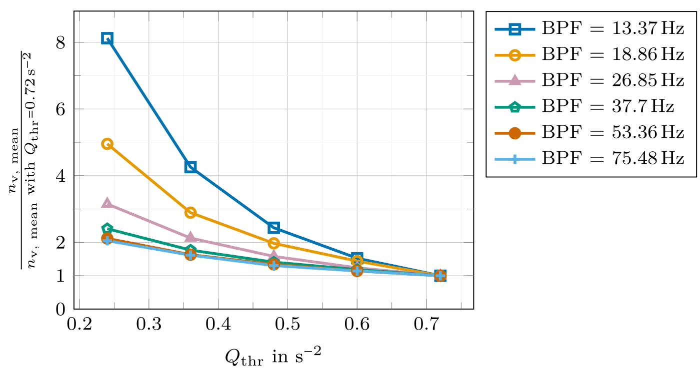

c) Influence of the vortex detection threshold Q_{thr} on $n_{\mathrm{v,\,mean}}$ in relation to $Q_{\mathrm{thr}} = 72 \times 10^4\ \mathrm{s}^{-2}$ for several blade passing frequencies at $-0.6\,z/R$

Fig. 19 Influence of BPF on blade tip vortex characteristics and secondary vortex appearance.

Acknowledgments

This project is funded by the Deutsche Forschungsgemeinschaft (DFG, German Research Foundation) through the project "Wirbelzerfall im rotierenden System" (Project ID: 490853673). The authors also acknowledge the fruitful discussions with our project partners from IAG Stuttgart, who performed numerical simulations on these cases. Additionally, the authors thank Markus Krebs and Florian Renneke for their contribution to the test stand.

References

[1] Chaderjian, N. M., and Buning, P. G., "High Resolution Navier-Stokes Simulation of Rotor Wakes," *Proceedings of the American Helicopter Society 67th Annual Forum*, Vertical Flight Soc., Fairfax, VA, 2011, pp. 1–18.

[2] Wolf, C. C., Schwarz, C., Kaufmann, K., Gardner, A. D., Michaelis, D., Bosbach, J., Schanz, D., and Schröder, A., "Experimental Study of Secondary Vortex Structures in a Rotor Wake," *Experiments in Fluids*, Vol. 60, No. 11, 2019, Paper 175.
https://doi.org/10.1007/s00348-019-2807-1

[3] Hariharan, N. S., Egolf, T. A., and Sankar, L. N., "Simulation of Rotor in Hover: Current State, Challenges and Standardized Evaluation," *52nd Aerospace Sciences Meeting, AIAA Paper 2014-0041*, American Inst. of Aeronautics and Astronautics, 2014.
https://doi.org/10.2514/6.2014-0041

[4] Potsdam, M., and Jayaraman, B., "UH-60A Rotor Tip Vortex Prediction and Comparison to Full-Scale Wind Tunnel Measurements," *Proceedings of the American Helicopter Society 70th Annual Forum*, 2014, pp. 1–21.

[5] Öhrle, C., Schäferlein, U., Keßler, M., and Krämer, E., "Higher-Order Simulations of a Compound Helicopter Using Adaptive Mesh Refinement," *Proceedings of the 74th Annual Forum of the American Helicopter Society*, American Helicopter Society, 2018, pp. 1–19.

[6] Jain, R., "Sensitivity Study of High-Fidelity Hover Predictions on the Sikorsky S-76 Rotor," *Journal of Aircraft*, Vol. 55, No. 1, 2018, pp. 78–88.
https://doi.org/10.2514/1.C034076

[7] Bodling, A., and Potsdam, M., "Numerical Investigation of Secondary Vortex Structures in a Rotor Wake," *Journal of the American Helicopter Society*, Vol. 67, No. 4, 2022, pp. 1–18.
https://doi.org/10.4050/JAHS.67.042007

[8] Egolf, T. A., Hariharan, N. S., Narducci, R. P., and Reed, E., "AIAA Standardized Hover Simulation: Hover Performance Prediction Status and Outstanding Issues," *55th AIAA Aerospace Sciences Meeting, AIAA Paper 2017-1429*, American Inst. of Aeronautics and Astronautics, 2017, pp. 1–17.
https://doi.org/10.2514/6.2017-1429

[9] Abras, J., Hariharan, N. S., and Narducci, R. P., "Wake Breakdown of High-Fidelity Simulations of a Rotor in Hover," *AIAA Scitech 2019 Forum, AIAA Paper 2019-0593*, American Inst. of Aeronautics and Astronautics, 2019.
https://doi.org/10.2514/6.2019-0593

[10] Schanz, D., Gesemann, S., and Schröder, A., "Shake-the-Box: Lagrangian Particle Tracking at High Particle Image Densities," *Experiments in Fluids*, Vol. 57, No. 5, 2016, Paper 70.
https://doi.org/10.1007/s00348-016-2157-1

[11] Schwarz, C., Bodling, A., Wolf, C. C., Brinkema, R., Potsdam, M., and Gardner, A. D., "Development of Secondary Vortex Structures in Rotor Wakes," *Experiments in Fluids*, Vol. 63, No. 1, 2022.
https://doi.org/10.1007/s00348-021-03348-8

[12] Bodling, A., Schwarz, C., Wolf, C. C., and Gardner, A. D., "Enhancing Numerical Accuracy in the Prediction of Rotor Wake Vortex Structures," *Physics of Fluids*, Vol. 36, No. 3, 2024, Paper 037137. https://doi.org/10.1063/5.0196010

[13] Thurman, C., Boyd, D. D., and Lopes, L. V., "Prediction of Broadband Blade-Wake Back-Scatter Noise from a Hovering Ideally Twisted Rotor Using OVERFLOW2-ANOPP2," *AIAA SCITECH 2024 Forum*, American Inst. of Aeronautics and Astronautics, 2024. https://doi.org/10.2514/6.2024-2471

[14] Scarano, F., and Poelma, C., "Three-Dimensional Vorticity Patterns of Cylinder Wakes," *Experiments in Fluids*, Vol. 47, No. 1, 2009, Paper 69. https://doi.org/10.1007/s00348-009-0629-2

[15] Williamson, C. H. K., "The Existence of Two Stages in the Transition to Three-Dimensionality of a Cylinder Wake," *Physics of Fluids*, Vol. 31, No. 11, 1988, pp. 3165–3168. https://doi.org/10.1063/1.866925

[16] Gibeau, B., Koch, C. R., and Ghaemi, S., "Secondary Instabilities in the Wake of an Elongated Two-Dimensional Body with a Blunt Trailing Edge," *Journal of Fluid Mechanics*, Vol. 846, 2018, pp. 578–604. https://doi.org/10.1017/jfm.2018.285

[17] Williamson, C. H. K., "Three-Dimensional Wake Transition," *Journal of Fluid Mechanics*, Vol. 328, 1996, pp. 345–407. https://doi.org/10.1017/S0022112096008750

[18] Holzäpfel, F., Misaka, T., and Hennemann, I., "Wake-Vortex Topology, Circulation, and Turbulent Exchange Processes," *AIAA Atmospheric and Space Environments Conference, AIAA Paper 2010-7992*, American Inst. of Aeronautics and Astronautics, 2010. https://doi.org/10.2514/6.2010-7992

[19] Bernal, L. P., and Roshko, A., "Streamwise Vortex Structure in Plane Mixing Layers," *Journal of Fluid Mechanics*, Vol. 170, 1986, pp. 499–525. https://doi.org/10.1017/S002211208600099X

[20] Wassermann, P., and Kloker, M., "Mechanisms and Passive Control of Crossflow-Vortex-Induced Transition in a Three-Dimensional Boundary Layer," *Journal of Fluid Mechanics*, Vol. 456, 2002, pp. 49–84. https://doi.org/10.1017/S0022112001007418

[21] Bell, J. H., and Mehta, R. D., "Measurements of the Streamwise Vortical Structures in a Plane Mixing Layer," *Journal of Fluid Mechanics*, Vol. 239, No. 1, 1992, Paper 213. https://doi.org/10.1017/S0022112092004385

[22] Leweke, T., Le Dizès, S., and Williamson, C. H., "Dynamics and Instabilities of Vortex Pairs," *Annual Review of Fluid Mechanics*, Vol. 48, No. 1, 2016, pp. 507–541. https://doi.org/10.1146/annurev-fluid-122414-034558

[23] Bodling, A., Schwarz, C., Wolf, C. C., and Gardner, A. D., "Numerical and Experimental Assessment of Parameters Influencing the Development of Secondary Vortex Structures in Rotor Wakes," *Proceedings of the Vertical Flight Society 79th Annual Forum, Vertical Flight Society*, 2023, pp. 1–17. https://doi.org/10.4050/F-0079-2023-17995

[24] Schröder, D., Leweke, T., and Stumpf, E., "High-Speed Volumetric Particle Tracking Measurements of Unstable Helical Vortex Pairs," *Experiments in Fluids*, Vol. 64, No. 8, 2023, Paper 141. https://doi.org/10.1007/s00348-023-03679-8

[25] Heineck, J. T., Yamauchi, G. K., Wadcock, A. J., Lourenco, L. M., and Abrego, A., "Application of Three-Component PIV to a Hovering Rotor Wake," *Annual Forum Proceedings-American Helicopter Society*, Vol. 56, American Helicopter Society, Fairfax, VA, 2000, pp. 375–390.

[26] Ramasamy, M., Johnson, B., and Leishman, J. G., "Turbulent Tip Vortex Measurements Using Dual-Plane Stereoscopic Particle Image Velocimetry," *AIAA Journal*, Vol. 47, No. 8, 2009, pp. 1826–1840. https://doi.org/10.2514/1.39202

[27] Mula, S. M., Stephenson, J. H., Tinney, C. E., and Sirohi, J., "Dynamical Characteristics of the Tip Vortex from a Four-Bladed Rotor in Hover," *Experiments in Fluids*, Vol. 54, No. 10, 2013, Paper 1600. https://doi.org/10.1007/s00348-013-1600-9

[28] Raffel, M., Bauknecht, A., Ramasamy, M., Yamauchi, G. K., Heineck, J. T., and Jenkins, L. N., "Contributions of Particle Image Velocimetry to Helicopter Aerodynamics," *AIAA Journal*, Vol. 55, No. 9, 2017, pp. 2859–2874. https://doi.org/10.2514/1.J055571

[29] Wieneke, B., "PIV Uncertainty Quantification from Correlation Statistics," *Measurement Science and Technology*, Vol. 26, No. 7, 2015, Paper 074002. https://doi.org/10.1088/0957-0233/26/7/074002

[30] van der Wall, B. G., and Richard, H., "Analysis Methodology for 3C-PIV Data of Rotary Wing Vortices," *Experiments in Fluids*, Vol. 40, No. 5, 2006, pp. 798–812. https://doi.org/10.1007/s00348-006-0117-x

[31] Bauknecht, A., Ewers, B., Schneider, O., and Raffel, M., "Aerodynamic Results from the STAR Hover Test: An Examination of Active Twist Actuation," *European Rotorcraft Forum*, 2015.

[32] Braukmann, J., Schwarz, C., Wolf, C., Buron, E., Koch, S., Buske, G., and Gardner, A., "BOS and Hot-Film Analysis of a CH-53G Helicopter Wake in Ground Effect," *Proceedings of the Vertical Flight Society 79th Annual Forum, Vertical Flight Society*, 2023, pp. 1–15. https://doi.org/10.4050/F-0079-2023-18181

[33] Quaranta, H. U., Bolnot, H., and Leweke, T., "Long-Wave Instability of a Helical Vortex," *Journal of Fluid Mechanics*, Vol. 780, 2015, pp. 687–716. https://doi.org/10.1017/jfm.2015.479

[34] Betz, A., and Prandtl, L., "Schraubenpropeller Mit Geringstem Energieverlust," *Nachrichten von der Gesellschaft der Wissenschaften zu Göttingen, Mathematisch-Physikalische Klasse*, Vol. 1919, No. 1, 1919, pp. 193–217.

[35] Luckring, J., "The Discovery and Prediction of Vortex Flow Aerodynamics," *Aeronautical Journal*, Vol. 123, No. 1264, 2019, pp. 729–804. https://doi.org/10.1017/aer.2019.43

[36] Meunier, P., and Leweke, T., "Elliptic Instability of a Co-Rotating Vortex Pair," *Journal of Fluid Mechanics*, Vol. 533, 2005. https://doi.org/10.1017/S0022112005004325

[37] Kocurek, J. D., and Tangler, J. L., "A Prescribed Wake Lifting Surface Hover Performance Analysis," *Journal of the American Helicopter Society*, Vol. 22, No. 1, 1977, pp. 24–35. https://doi.org/10.4050/JAHS.22.24

A. Jones
Associate Editor